Research Square

Preprints are preliminary reports that have not undergone peer review.
They should not be considered conclusive, used to inform clinical practice,
or referenced by the media as validated information.

PEC-backed absorber for multiband applications ranging from 8 GHz to 40 GHz

Sakshi Sharma

ee23d501@iittp.ac.in

Indian Institute of Technology Tirupati

Sai Haranadh Akkapanthula

Indian Institute of Technology Tirupati

Srujana Kagita

Indian Institute of Technology Tirupati

Research Article

Keywords: Metasurface, split-ring resonator, multi-notch transmission, equivalent circuit, coupled resonator, polarization-insensitive, electromagnetic coupling, multilayer metasurface

Posted Date: November 13th, 2026

DOI: https://doi.org/10.21203/rs.3.rs-11228830/v1

License: This work is licensed under a Creative Commons Attribution 4.0 International License.
Read Full License

Additional Declarations: No competing interests reported.

PEC-backed absorber for multiband applications ranging from 8 GHz to 40 GHz

Sakshi Sharma[1], Sai Haranadh Akkapanthula[1], and Srujana Kagita[1]
[1]Indian Institute of Technology, Tirupati, 517619, India.
Corresponding author: Sakshi Sharma (ee23d501@iittp.ac.in)

***Abstract*—In this paper, a compact multi-ring metasurface is proposed for multi-notch transmission over a wide frequency range of 8–40 GHz. The structure consists of concentric split-ring resonators with different radii and auxiliary coupling rings, where the resonant response is controlled by the effective inductance, capacitance, and electromagnetic coupling between the resonating elements. The design is developed through a nine-stage evolution, and an equivalent coupled-RLC model is used to explain the origin of the observed resonances. The structure also exhibits similar responses under TE and TM polarizations, indicating polarization-insensitive behavior. Further, the effects of stacking, relative displacement, air-gap separation, and rotation between metasurface layers are investigated, demonstrating additional control over the resonant transmission characteristics.**

***Index Terms*—Metasurface, split-ring resonator, multi-notch transmission, equivalent circuit, coupled resonator, polarization-insensitive, electromagnetic coupling, multilayer metasurface.**

I. INTRODUCTION

Metasurfaces have attracted considerable interest for controlling the transmission, reflection, and propagation of electromagnetic (EM) waves using electrically small and periodically arranged metallic or dielectric elements. Compared with conventional three-dimensional metamaterials, planar metasurfaces provide a compact and relatively simple platform for realizing frequency-selective and wave-manipulation functions at microwave and millimeter-wave frequencies [1], [2]. Their response can be controlled by properly selecting the shape, dimensions, and arrangement of the unit-cell elements. In particular, ring-based resonators are widely used in microwave structures because their resonant behavior can be controlled through the current path, split gaps, and coupling between adjacent elements [3], [4].

Split-ring resonators (SRRs) provide a convenient way of obtaining strong electromagnetic resonance in a compact area. The resonance of an SRR can be represented using an equivalent LC model, where the metallic path mainly contributes to the effective inductance and the split region provides the dominant capacitive contribution [3]–[5],[17],[20],[21]. The resonant frequency is therefore approximately determined by $f_r = 1/2\pi\sqrt{LC}$. Equivalent-circuit models have been widely used to describe the behavior of SRRs and their coupling with microwave transmission structures, providing a useful link between the physical geometry and the measured or simulated transmission response [3], [5],[23]. In addition to the self-resonance of individual rings, the electromagnetic interaction between neighboring resonators can significantly modify the response. The coupling may lead to resonance shifts, mode splitting, and the generation of closely spaced resonant frequencies. Such coupled-resonator behaviour has been used in the development of compact microwave filters, frequency-selective surfaces, and multi-band metamaterial structures [4], [6], [22].

The use of multiple resonating elements is effective for obtaining several transmission notches over a broad frequency range [17],[18],[24],[29],[30]. By using resonators with different electrical path lengths, different resonant frequencies can be achieved within a single unit cell. For circular resonators, the approximate current-path length is related to the ring radius by $L \approx 2\pi R$. However, the response of a practical multi-ring structure is also influenced by the split gaps, inter-ring spacing, connecting sections, dielectric environment, and electromagnetic coupling. Therefore, the final transmission response results from the combined interaction of the resonating elements rather than from an individual ring alone. An equivalent coupled-resonator model is useful for relating these geometrical parameters to the observed resonances [3], [5], [7].

Polarization stability is also important for practical metasurface applications. Circular and rotationally symmetric resonators can provide similar responses for different polarization states because their geometry reduces the dependence on the incident electric-field direction [8], [9],[25],[26],[27], [28]. In addition, multilayer metasurfaces provide further control of the transmission response through interlayer electromagnetic coupling. The relative displacement, separation, and angular orientation of the layers can modify this coupling and consequently change the resonant characteristics [9], [10].

In this work, a compact PEC-backed multi-ring absorptive metasurface is developed. The structure consists of concentric rings with R_1=5.5 mm, R_2=4 mm, and R_3=2.1 mm, together with smaller resonating elements having R_4=1 mm and R_5=0.7 mm. The different current-path lengths, split gaps, and inter-ring spacing provide multiple resonant paths and control the electromagnetic coupling, resulting in several transmission notches over the 8–40 GHz range.

An equivalent coupled-RLC network is developed to explain the resonant behavior and its relationship with physical geometry. The transmission characteristics are evaluated under TE and TM polarizations to investigate the polarization-insensitive response. Furthermore, stacked metasurface configurations are studied by varying the relative displacement, interlayer air gap, and rotation

angle. The measured results are compared with full-wave simulations to validate the proposed design and demonstrate the effect of geometrical and stacking parameters on the transmission characteristics. The proposed circuit was fabricated using an FR-4 substrate having a thickness of 1.58 mm, relative permittivity (ε_r) of 4.3, and loss tangent (tan δ) of 0.025. Simulations have been carried out using the CST microwave studio suite. Section II provides details of the design. In Section III, results have been discussed for single-layer, multilayer, angular and linear displacement of stacked-layer metasurfaces for TE and TM configurations.

II. DESIGN

A. Design evolution of the proposed metasurface

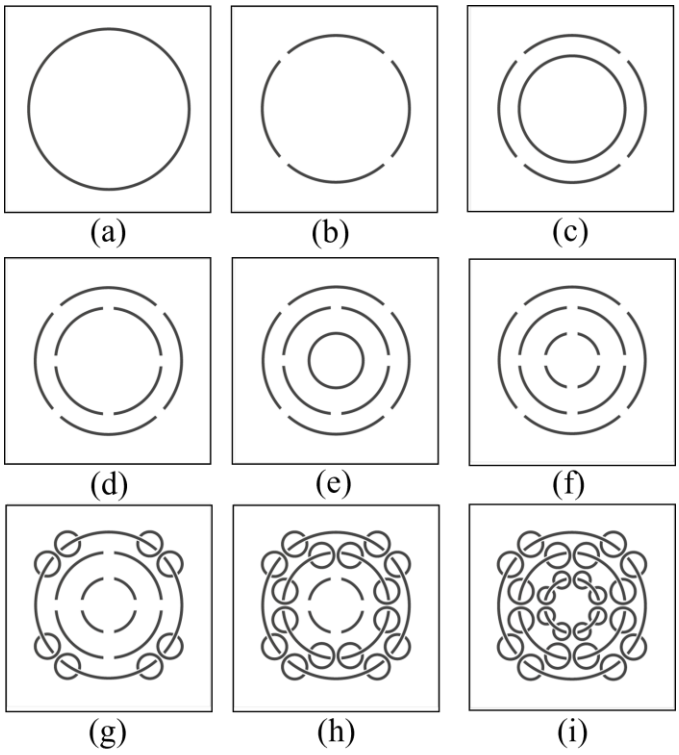


Fig. 1. Stepwise design evolution of the proposed PEC-backed metasurface: (a) Design-1 (b) Design-2 (c) Design-3 (d) Design-4 (e) Design-5 (f) Design-6 (g) Design-7 (h) Design-8 (i) Final Design

The proposed metasurface is developed as shown in Fig. 1 through a nine-stage design evolution, from Design-1 to the Final Design, to obtain a multi-notch transmission (Tx) response as shown in Fig. 2 over the 8–40 GHz frequency range. Design-1 consists of a single continuous outer ring and shows an isolated transmission dip near 30 GHz. In Design-2, cross-cuts with a gap of K_1=0.8 mm are introduced in the outer ring, converting it into a split-ring resonator. The introduced gap provides additional capacitive loading and shifts the fundamental resonance toward a lower frequency. Design-3 and Design-4 introduce a second concentric ring with R_2=4.0 mm, first without a split and then with a gap of K_2=0.8 mm. The addition of this ring introduces another resonant path, while the small spacing of G_1=0.2 mm between the adjacent rings results in electromagnetic coupling and produces additional transmission notches.

The design is further developed in Design-5 and Design-6 by introducing a third split-ring resonator with R_3=2.1 mm and K_3=0.8 mm. The additional resonant path increases the number of transmission notches, particularly in the 20–40 GHz frequency range. In Design-7 and Design-8, small peripheral coupling rings and interconnecting sections defined by M_1 and G_1–G_3 are added between the concentric rings. These elements introduce additional inductive and capacitive effects and increase the electromagnetic coupling between the resonating sections, resulting in further shifts and splitting of the existing resonances. At the end, the final design combines the complete nested ring configuration with the optimized radii, gap dimensions, and interconnecting sections. The geometry of the proposed final design is shown in Fig.3. The resulting transmission response exhibits several closely spaced resonant notches over the 8–40 GHz frequency range, demonstrating that the number and arrangement of the resonating rings, together with their gaps and coupling regions, strongly influence the overall multi-band transmission characteristics of the proposed metasurface.

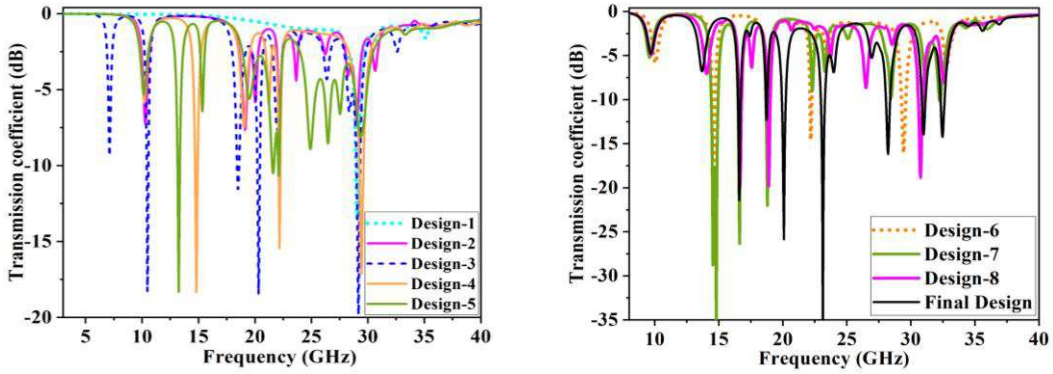


Fig. 2. Tx response of various design structures: (a) Design-1 to Design-5, (b) Design-6 to Final Design

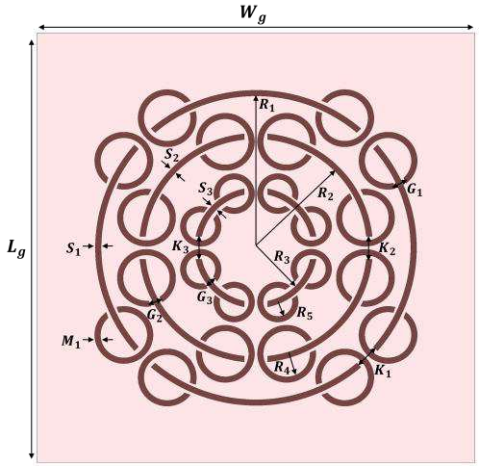


Fig. 3. Geometry of the proposed design multiring coupled metasurface; the dimensions of the proposed structure (in mm) Wg=15, Lg=15, R_1 = 5.5, R_2=4, R_3=2.1, R_4 = 1, R_5 = 0.7, G_1=G_2=G_3=0.4, K_1=K_2=K_3=0.8, S_1=S_2=S_3=0.2, M_1=0.2.

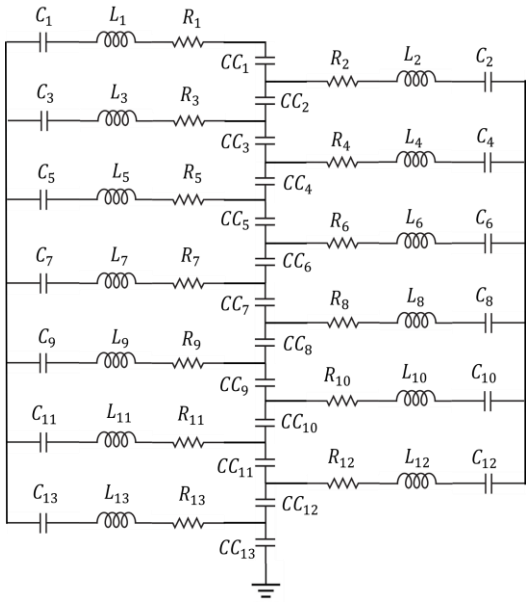
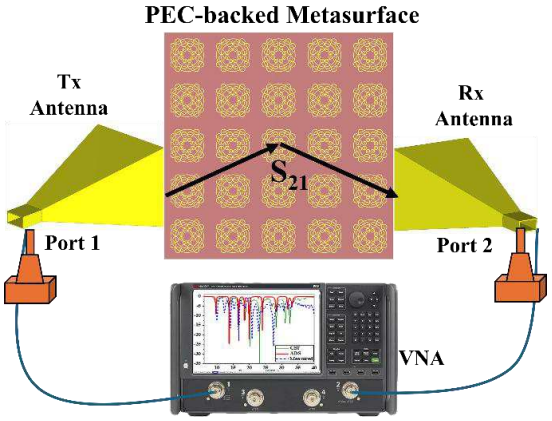


Fig. 4. Equivalent circuit of the proposed metasurface developed in ADS

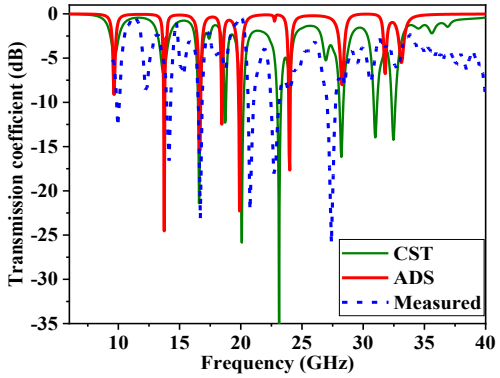
TABLE I

DESIGN PARAMETERS OF THE EQUIVALENT CIRCUIT OF THE METASURFACE

S.No.	Parameters	Value (pF)	Parameters	Value (nH)	Parameters	Value (ohm)	Parameters	Value (pF)
1.	C_1	0.0082	L_1	33.22	R_1	24	CC_1	1.50
2.	C_2	0.0029	L_2	32	R_2	35.25	CC_2	0.07
3.	C_3	0.0033	L_3	42.9	R_3	35.25	CC_3	0.2
4.	C_4	0.0022	L_4	34.8	R_4	35.25	CC_4	0.075
5.	C_5	0.0024	L_5	28.2	R_5	50	CC_5	0.025
6.	C_6	0.0016	L_6	30.36	R_6	29.25	CC_6	0.03
7.	C_7	0.0015	L_7	32.5	R_7	11.75	CC_7	0.075
8.	C_8	0.0018	L_8	20.5	R_8	75	CC_8	0.005
9	C_9	0.0029	L_9	13	R_9	1	CC_9	0.035
10.	C_{10}	0.033	L_{10}	50.48	R_{10}	19.45	CC_{10}	0.006
11.	C_{11}	0.004	L_{11}	32.53	R_{11}	37.6	CC_{11}	0.045
12.	C_{12}	0.017	L_{12}	31.36	R_{12}	31.2	CC_{12}	0.04
13.	C_{13}	0.0013	L_{13}	19.15	R_{13}	35.25	CC_{13}	0.03



(a)



(b)

Fig. 5. (a). Schematic of the testing setup of the PEC-backed metasurface (b) Comparative study of the equivalent circuit, CST simulation, and measured results

To investigate the physical mechanisms responsible for the multi-band Tx response, the evolution of the proposed metasurface is analysed in terms of the geometrical and equivalent-circuit parameters of the concentric ring resonators [2][11][12]. Fig.4 shows the equivalent circuit of the proposed metasurface. Fig.5(a) shows the test setup for measurement, and Fig.5(b) represents the comparative study of the S_{21} response of the equivalent circuit model developed in ADS, CST simulation and measured results. Table. I show the parameters used to design the equivalent circuit model of the proposed metasurface. Here, each circular metallic path can be represented by an effective inductance L_i, which is mainly determined by its mean radius and conductor width. For a circular conductor, the inductance can be approximated as [11],

$$L_i \approx \mu_0 R_i \left[ln\left(\frac{8R_i}{w}\right) - 2 \right] \quad (1)$$

where μ_0 is the permeability of free space, R_i is the mean radius of the resonator, and w is the conductor width. Thus, the larger rings provide longer current paths and higher effective inductive contributions. In Design-1, the initial continuous circular ring

with R_1=*5.5 mm* forms the primary resonating path and produces a distinct transmission minimum. As the structure is progressively modified, physical gaps are introduced into the metallic paths. These gaps interrupt the continuous current flow and produce localized electric-field concentration, resulting in an additional capacitive contribution to the resonator [12]. The corresponding gap capacitance is represented as,

$$C_{g,i} \approx \varepsilon_0 \varepsilon_{eff} \frac{wt}{G_i} + C_{fringe} \tag{2}$$

where ε_{eff} is the effective dielectric constant, t is the conductor thickness, and C_{fringe} represents the contribution from fringing fields. The combination of the effective inductance and gap capacitance forms an LC resonant path, whose resonance frequency can be approximated by [2] [13],

$$f_{r,i} = \frac{1}{2\pi\sqrt{L_i(C_{g,i}+C_{c,i})}} \tag{3}$$

Additionally, the radial spacing between adjacent rings provides mutual capacitive coupling $C_{c,i}$ [14].

Further modification of the structure introduces the inner rings and the smaller resonating elements with R_2=4 mm, R_3=2.1 mm, R_4=1 mm, and R_5=0.7 mm. The corresponding circular path lengths, estimated from $L_i=2\pi R$, are 25.13, 13.19, 6.28, and 4.40 mm, respectively, in addition to 34.56 mm for the outer ring R_1. These different path lengths provide different effective inductive contributions and allow the resonating sections to respond over different frequency regions. The smaller ring elements are connected to the outer, middle rings, and inner rings. The small radial spacing between adjacent resonating elements (S_1=S_2=S_3=0.2 mm) results in strong electric interaction between the neighbouring rings and can be represented by coupling capacitances $C_{c,i}$ in the equivalent circuit [14]. The additional dimensions K_1=K_2=K_3=0.8 mm further define the spacing and connecting metallic regions and consequently influence the current distribution and coupling strength. In Fig. 5, the lumped-circuit model simulation in ADS and 3D electromagnetic simulations in CST show deep resonances between 32 to 35 GHz. In the fabricated prototype, measured results in this frequency range have relatively shallow dips. This is due to the fabrication tolerances in obtaining small split rings of radius 0.7mm and slot width of 0.4mm. The deviation in measured results at high frequency bands is attributed to this factor.

As observed in the transmission response, the successive addition and modification of these resonating sections from Design-1 to Design-9 introduce new transmission minima and shift the existing resonances. This behaviour confirms that the observed resonances are not due to completely independent rings; rather, they result from the interaction of multiple resonant paths. In the final configuration, the combined effect of the different L_i–C_i resonant sections and the inter-ring coupling produces several closely spaced resonant modes over the investigated frequency range. Hence, the design evolution provides a direct relationship between the geometrical arrangement of the concentric and auxiliary rings and the resulting multi-band transmission characteristics. Therefore, the final response is not determined by the ring radius alone but by the combined effect of the resonator dimensions, gap capacitance, substrate loading, and electromagnetic coupling between the different sections.

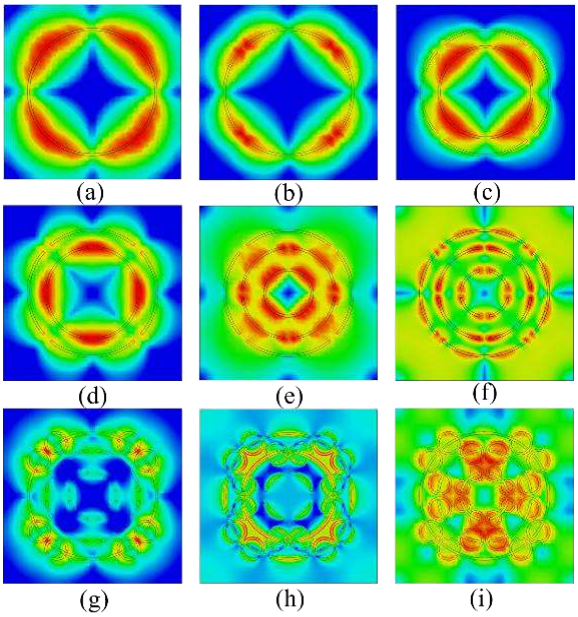


Fig. 6. E-field for (a) Design-1 at 9.5 GHz, (b) Design-2 at 9.9 GHz, (c) Design-3 at 13.6 GHz, (d) Design-4 at 13.68 GHz, (e) Design-5 at 21.2 GHz, (f) Design-6 at 21.9 GHz, (g) Design-7 at 22.8 GHz, (h) Design-8 at 24.3 GHz, (i) Final design at 26 GHz

The evolution of the resonant modes was further examined from the electric-field distributions shown in Fig.6. of Design-1 to the final design. Design-1 exhibits a dominant field concentration around the outer ring at 9.5 GHz, indicating that the fundamental mode is mainly associated with the larger resonating path. After introducing the cuts in Design-2, the corresponding resonance changes only slightly from 9.5 to 9.9 GHz, indicating that the introduced cuts provide a relatively small perturbation to the dominant mode. A similar behaviour is observed for Design-3 and Design-4, where the resonant frequency changes only from 13.60 to 13.68 GHz after introducing the additional cut. This small frequency variation suggests that the dominant mode is not significantly altered by the cut, while the field distribution remains mainly associated with the same resonating region. With further addition of concentric rings and coupling sections from Design-5 to Final design, the field distribution progressively involves multiple resonating elements, and the dominant resonance shifts toward higher frequencies. These results indicate that the evolution of the structure modifies the modal distribution through changes in the effective inductance, capacitance, and electromagnetic coupling between the resonating elements [3], [7], [15].

The electromagnetic interaction between adjacent resonating rings results in coupling and can modify the resonant frequencies of the structure. When two coupled resonators have similar resonance frequencies, the interaction produces two split resonant modes at f_L and f_H. The coupling coefficient can be estimated from these frequencies as [7][16], [17]

$$k = \frac{f_H^2 - f_L^2}{f_H^2 + f_L^2} \tag{4}$$

where f_L and f_H are the lower and higher coupled-resonance frequencies, respectively. A larger frequency splitting (f_H - f_L) indicates stronger electromagnetic coupling, whereas a smaller splitting indicates weaker coupling. However, two closely spaced S_{21} dips cannot automatically be considered a coupled pair, since they may originate from different resonating elements. Therefore, the corresponding surface-current distributions are examined to identify the interacting modes. For the proposed multi-ring structure, this analysis is used to relate the observed resonance splitting to the electromagnetic coupling between the concentric rings. Table II shows the calculated coupling coefficient for the evaluated design.

TABLE II
COUPLING COEFFICIENT OF THE EVALUATED DESIGN

Design	f_L (GHz)	f_H (GHz)	Coupling Factor (k)	Coupling Regime
Design-1	---	29.056	0	**Uncoupled:** Single ring with one dominant resonance.
Design-2	---	10.284	0	**Uncoupled:** Split ring shifts the resonance to lower frequency.
Design-3	7.130	10.474	0.354	**Initial coupling:** Concentric rings introduce mode splitting.
Design-4	10.208	14.844	0.358	**Strong coupling:** Increased interaction between ring sections.
Design-5	10.170	13.248	0.258	**Moderate coupling:** Added element reduces the mode splitting.
Design-6	14.616	22.178	0.394	**Strongest coupling:** Multiple rings produce strong interaction.
Design-7	14.540	14.806	0.018	**Weak coupling:** Closely spaced modes indicate weak interaction.
Design-8	9.714	13.932	0.346	**Strong coupling:** Ring arrangement increases electromagnetic interaction.
Design-9 (Final)	16.592	23.128	0.320	**Strong coupling:** Nested rings provide significant interaction.

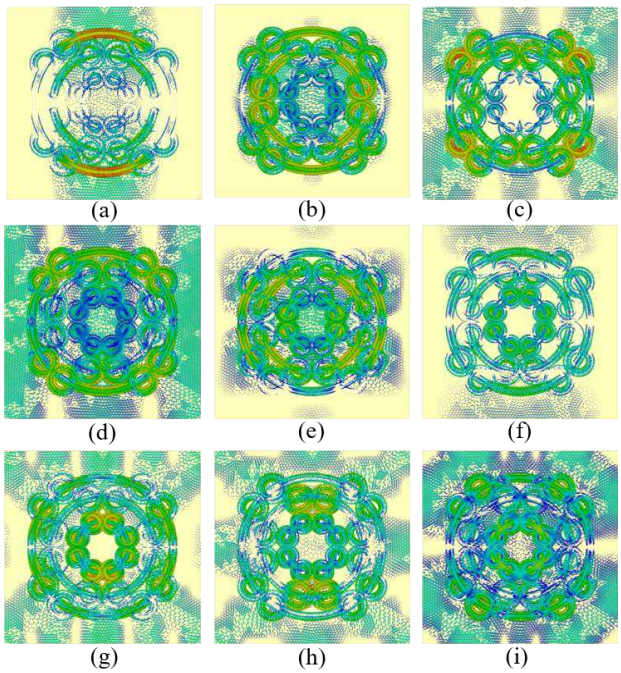


Fig. 7. Surface Current distribution of the proposed design at (a) 9.7 GHz, (b) 13.7 GHz, (c) 16.6 GHz, (d) 18.7 GHz, (e) 20.08 GHz, (f) 23.128 GHz, (g) 28.2 GHz, (h) 31 GHz, and (i) 32.5 GHz.

The resonant modes of the proposed multi-ring metasurface are investigated from the surface-current distributions corresponding to the transmission minima in Fig.7. The resonance of an individual resonating section can be approximately described by equation (3), [3]. Since the proposed structure contains multiple concentric and peripheral resonating sections with different dimensions and small separation gaps, electromagnetic coupling occurs between the resonators, resulting in collective or hybridized resonant modes rather than completely independent ring resonances. In general, the coupled-mode frequencies can be expressed as,

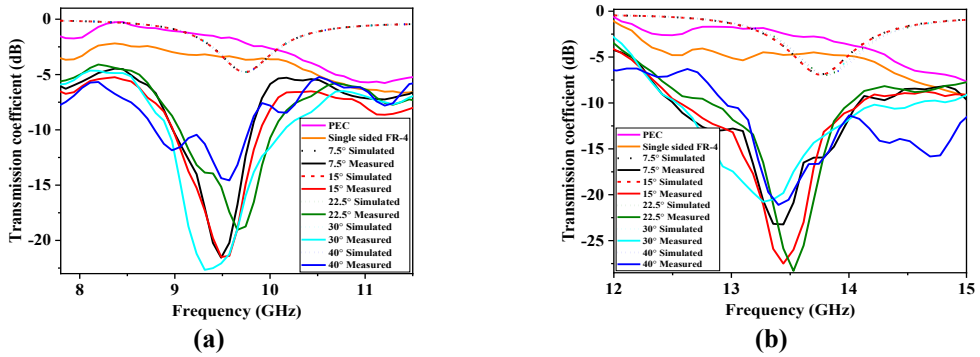
$$\omega_{\pm} = \frac{\omega_1+\omega_2}{2} \pm \sqrt{\left(\frac{\omega_1-\omega_2}{2}\right)^2 + |K|^2} \tag{5}$$

where $\omega_1$and $\omega_2$are the uncoupled resonant frequencies and K represents the coupling strength [7]. The surface-current distributions provide the spatial signature of these resonant modes.

At 9.714 GHz, the current is mainly concentrated along the larger outer resonating paths, indicating a longer effective current path and consequently a lower-frequency resonant mode. With increasing frequency, the current progressively involves the intermediate, inner, and peripheral resonating sections, producing different modal current distributions. In the 18.72–23.13 GHz range, the current is distributed over multiple rings and connecting sections, confirming stronger participation of the coupled resonating elements. At 28.22, 30.99, and 32.48 GHz, the current becomes more concentrated around the smaller resonating sections, which support higher-frequency modes because of their shorter effective current paths. Thus, the distinct surface-current distributions observed at the nine S_{21} notches confirm that the multi-notch response originates from different collective resonant modes of the complete coupled structure, while variations in the current distribution arise from changes in the effective inductance, capacitance, and electromagnetic coupling between the resonating elements [3][7][15].

III. Results and Discussion

A. TE and TM mode response



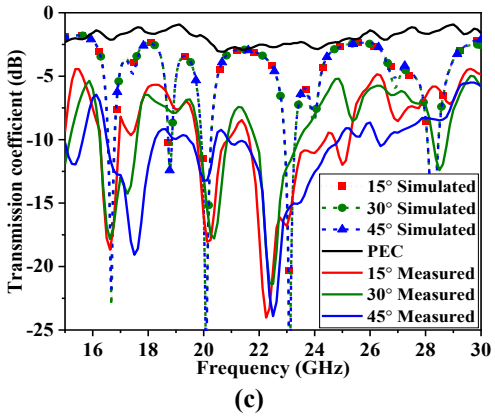


Fig. 8. Transmission coefficient for TE mode at 8 to 30 GHz for different angles: (a) 1st band at 9.7 GHz, (b) 2nd band at 13.8 GHz, (C) three bands at 16.7 GHz, 20.1 GHz and 23 GHz in the 15 to 30 GHz band

The transmission characteristics of the proposed metasurface were investigated under both TE and TM polarization to evaluate its multi-band response and polarization-insensitive behavior. Fig. 8 presents the simulated and measured transmission coefficients for TE polarization over the frequency range of 8–30 GHz. The proposed structure exhibits several distinct transmission dips at approximately 9.7, 13.8, 17.0, 20.1, and 23 GHz. These resonances are produced by the different resonating sections of the circular-ring structure and their electromagnetic interaction. The response of the single-sided FR-4 substrate is also included for comparison, while the PEC response provides a reference for the transmission characteristics of an ideally conducting surface.

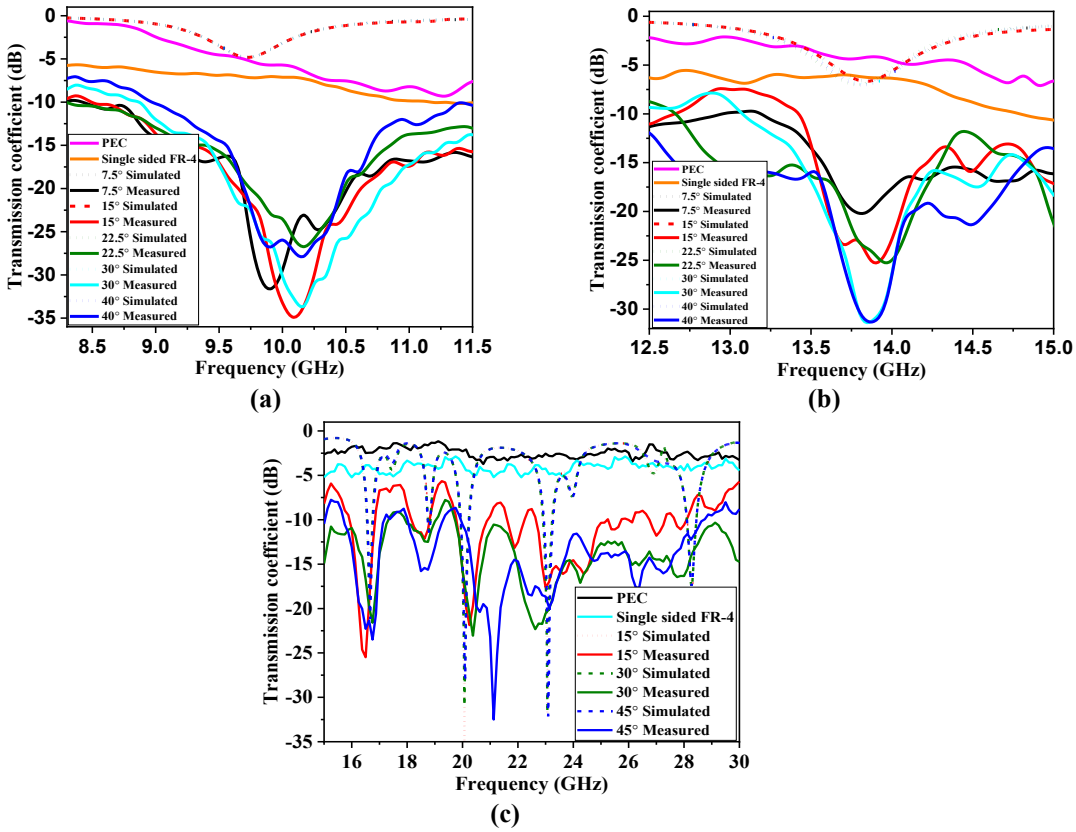


Fig. 9. Transmission coefficient for TM mode at 8 to 30 GHz (a) 1st band at 9.7 GHz (b) 2nd band at 13.8 GHz (C) three band 16.7 GHz, 20.1 GHz and 23 GHz at 15 to 30 GHz band

Fig. 9 shows the corresponding transmission response under TM polarization. The main resonances are observed at approximately 9.7, 13.8, 16.7, 20.1, and 23 GHz, with additional resonant features appearing over the higher frequency range. A close correspondence between the TE and TM responses can be observed, particularly for the main resonant frequencies. The resonances around 9.7, 13.8, 20.1, and 23 GHz remain nearly unchanged when the polarization is changed from TE to TM, while only small variations in resonance depth and frequency are observed. This stable resonant behavior for the two orthogonal polarization states is attributed to the circular and symmetric arrangement of the resonating elements. The similar transmission characteristics obtained for TE and TM polarization confirm the polarization-insensitive nature of the proposed metasurface.

B. Multilayered metasurface: Effect of Stacking the Metasurface Sheets

(a) Case-1

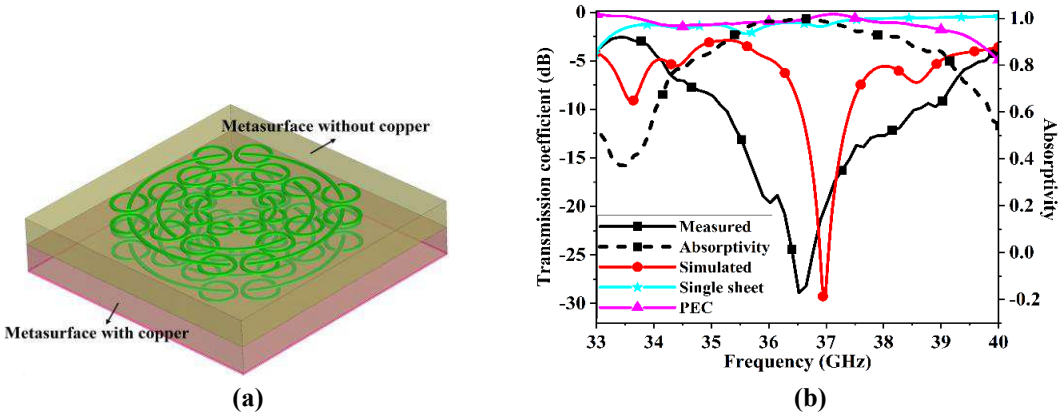


Fig. 10. Layered metasurface: (a) Stacked 2 metasurface sheets with no air gap (b) Tx coefficient and Absorptivity response for the double-layered metasurface working at 37 GHz

To further investigate the effect of multilayer configuration, two metasurface sheets were stacked, and their transmission response was studied. Fig. 10 shows the configuration in which two metasurface sheets are placed one above the other. The simulated and measured responses show a pronounced resonance around 37 GHz. Compared with the response of a single sheet, the stacked configuration produces a stronger change in the transmission coefficient because the electromagnetic fields interact with both metasurface layers. The coupling between the two sheets modifies the effective inductance and capacitance of the overall structure, resulting in a shift and enhancement of the resonant response.

(b) Case-2

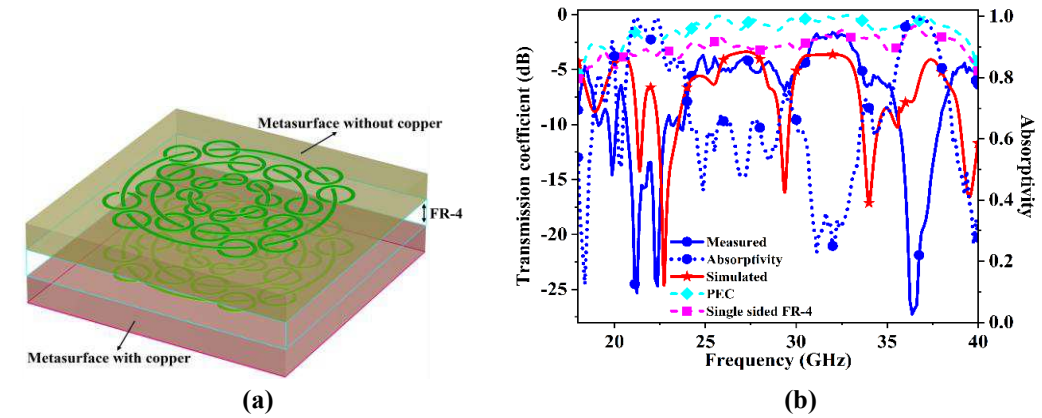


Fig. 11. Layered metasurface: (a) FR-4 plain sheet stacked between the 2 metasurface sheets (b) Tx coefficient and Absorptivity response at 34 GHz, 29.4 GHz and 22.7 GHz

The effect of introducing an FR-4 sheet between the two metasurface layers was investigated in Fig. 11. In this configuration, the plain FR-4 layer is placed between the two metallic metasurface sheets. The transmission response shows resonances at approximately 34, 29.4, and 27.2 GHz. The appearance of multiple resonant features indicates that the intermediate dielectric layer changes the electromagnetic interaction between the two metasurface sheets. In addition to increasing the effective dielectric loading, the FR-4 layer modifies the electric-field distribution between the sheets and consequently changes their coupling. As a result, the resonant frequencies are shifted compared with the directly stacked configuration. This confirms that the dielectric layer has a clear effect on the overall transmission characteristics.

C. Multilayered metasurface: *Effect of Air Gap Between the Metasurface Sheets*

(a) Case-1

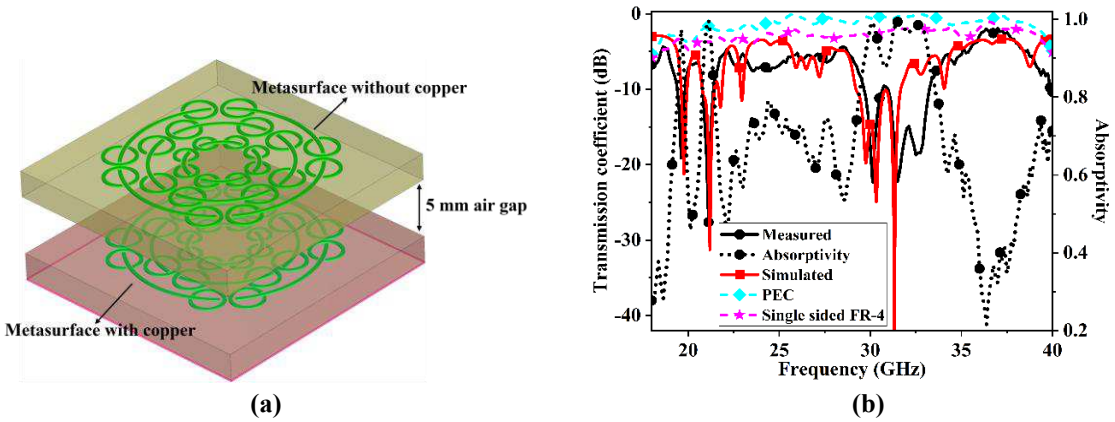


Fig. 12. Layered metasurface: (a) 5 mm air gap between 2 sheets (b) Tx coefficient and Absorptivity response at 31.3 GHz, 30.3 GHz, 21.2 GHz and 19.8 GHz

The influence of the separation between the metasurface sheets was further studied by introducing a 5-mm air gap, as shown in Fig. 12. In this case, the two metasurface sheets are physically separated by an air region instead of being directly stacked. The measured and simulated responses exhibit several resonant features around 31.3, 30.3, 21.2, and 19.8 GHz. The appearance of these resonances and their frequency positions are different from those obtained with the FR-4 intermediate layer. This behavior can be explained by the change in electromagnetic coupling between the two metasurface sheets. Increasing separation reduces the direct interaction between the layers and changes the effective capacitance and field distribution of the combined structure. Therefore, the air gap provides an additional parameter for controlling the resonant response.

(b) Case-2

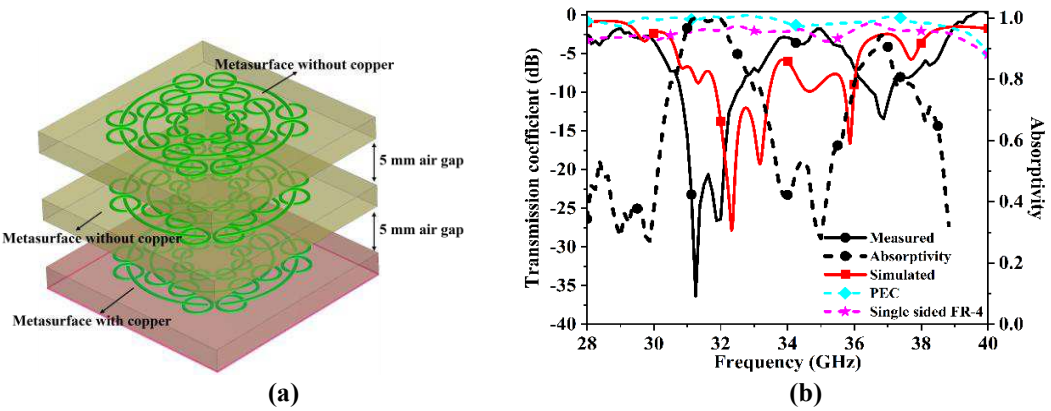


Fig. 13. Layered metasurface: (a) 5 mm air gap between 3 sheets (b) Tx coefficient and Absorptivity response at 32.4 GHz, 33.2 GHz, and 35.9 GHz.

The effect of increasing the number of metasurface layers was further examined in Fig. 13, where three metasurface sheets are separated using 5-mm air gaps. The measured and simulated responses show several resonances, with prominent features occurring around 32.4, 33.2, and 35.9 GHz. Compared with the two-layer configuration, the addition of a third metasurface sheet introduces further electromagnetic interaction and increases the number of coupled resonant modes. The resulting response is therefore governed by the combined interaction among the three metasurface layers rather than by the response of an individual sheet.

D. Multilayered metasurface: *Effect of Linear and angular displacement between the two stacked metasurface sheets*

(a) Case-1

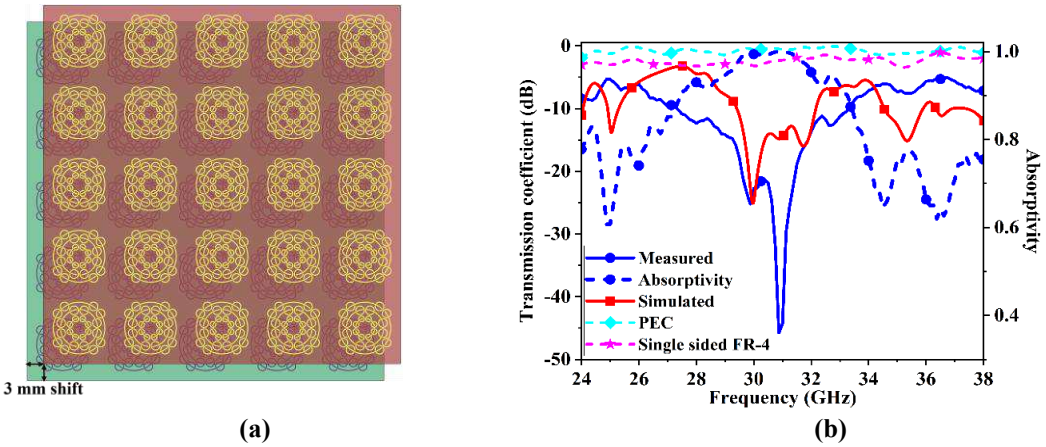


Fig. 14. Layered metasurface: (a) sheet shifted 3 mm diagonally (b) Tx coefficient and Absorptivity response at 30 GHz

Fig. 14 presents the transmission response of the double-stacked metasurface when one sheet is shifted by 3 mm along the diagonal direction with respect to the other sheet. The measured and simulated responses show a pronounced transmission minimum around 30 GHz, indicating that the displacement can change the resonant behavior of the stacked structure. The resonance remains clearly identifiable after the displacement, showing that the proposed structure maintains its resonant response under a small positional shift. This result also indicates that the electromagnetic coupling between the two sheets is affected by the relative displacement, leading to a slight change in the resonance characteristics.

(b) Case-2

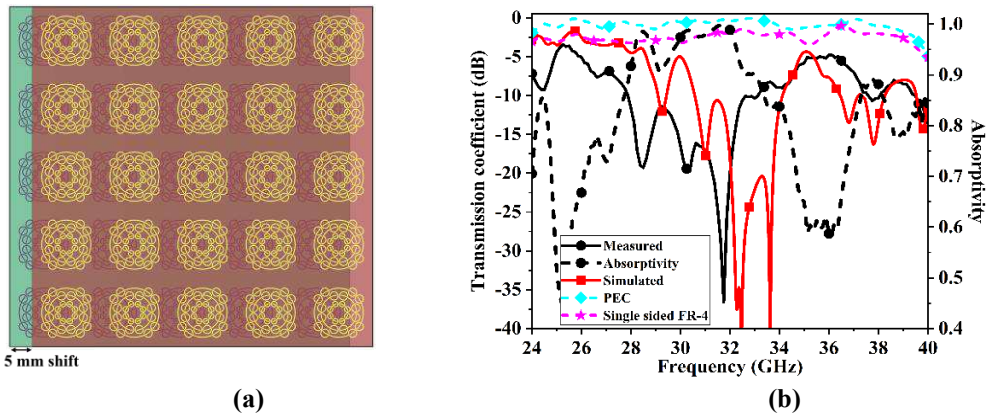
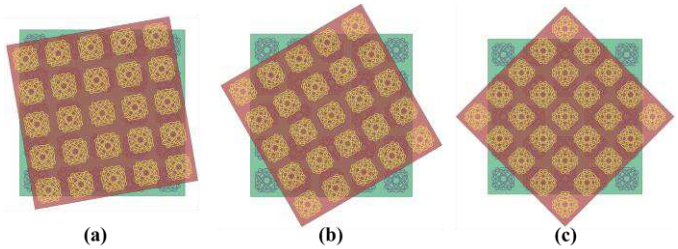
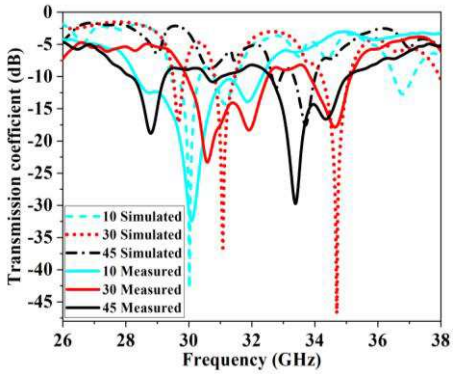


Fig. 15. Layered metasurface: (a) Double-stacked with 5mm displacement (b) Tx coefficient and Absorptivity response at 32.3 GHz

Fig. 15 shows the transmission response when the relative diagonal displacement between the two metasurface sheets is increased to 5 mm. In comparison with the 3-mm displacement case, the larger separation between the corresponding resonating elements produces a noticeable change in the transmission characteristics. Several resonant features appear in the 28–34 GHz region, with a prominent resonance observed around 32.3 GHz. These changes are mainly associated with the variation in electromagnetic coupling caused by the increased relative displacement between the two sheets. The result confirms that the relative position of the stacked layers can be used to modify the resonant transmission response.

(c) Case-3





(b)

Fig. 16. Two stacked sheets at different rotation angles: (a) 10°, (b) 30°, (c) 45°, and (d) transmission response

Fig. 16 presents the transmission response of the double-stacked metasurface for different relative rotation angles of 10∘, 30∘, and 45∘. The corresponding simulated and measured responses show that the resonant frequencies and transmission levels vary with the rotation angle. As the upper metasurface is rotated, the relative position of the resonating elements changes, which modifies the electromagnetic coupling between the two layers. Consequently, the resonance positions and their corresponding transmission depths change over the investigated frequency range. The measured results show the same general trend as the simulated responses, with some differences arising from practical measurement conditions. These results demonstrate that the stacked metasurface is sensitive to the relative angular orientation of the two sheets.

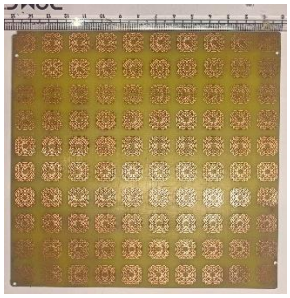


Fig.17. Fabricated circuit of the proposed metasurface

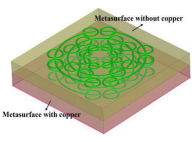


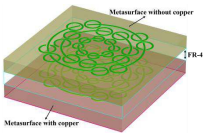
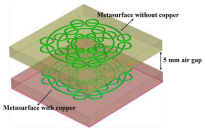
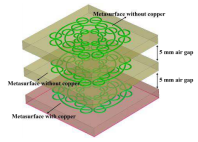
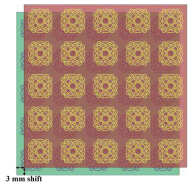
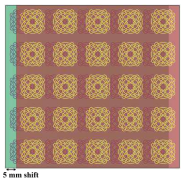
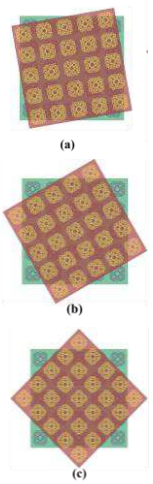
Fig. 18. Experimental setup of the proposed metasurface

The proposed metasurface was experimentally characterized using the fabricated prototype shown in Fig. 17. The fabricated sample consists of a 10×10 periodic array of the proposed unit cells on the dielectric substrate. The transmission characteristics were measured in an anechoic chamber using two horn antennas positioned on opposite sides of the metasurface, as shown in Fig. 18. Measurements were carried out using Keysight PNA N5224B vector network analyzer. Table III shows the comparative study of the various cases of the multilayer metasurface topologies.

TABLE III

COMPARATIVE STUDY OF THE VARIOUS MULTILAYER METASURFACE TOPOLOGIES

S. No.	Metasurface topology	Cases	Frequency (GHz)	Design	Description
1.	**Effect of the stacking:**	*Case-1*	37		Two Stacked metasurface sheets

		Case-2	22.7, 29.4, and 34 GHz		Three stacked metasurface sheets with plain FR-4 substrate
2.	**Effect of Air Gap Between the Metasurfaces**	*Case:1*	31.3, 30.3, 21.2 and 19.8		5 mm air gap between 2 sheets
		Case:2	32.4, 33.2, and 35.9.		5 mm air gap between 3 sheets
3.	**Effect of displacement and rotation between the two stacked metasurfaces**	*Case-1*	30 GHz		Sheet shifted 3 mm diagonally
		Case-2	32.3 GHz		Double-stacked with 5mm displacement
		Case-3	28 GHz to 34 GHz		Two stacked sheets at different rotation angle 10 30 and 45°

VI. Conclusion

A compact concentric coupled ring metasurface was developed for multi-notch transmission over the 8–40 GHz frequency range. The different ring sizes, split gaps, and coupling elements provide multiple resonant paths and control the overall transmission response. The equivalent RLC model successfully explains the resonant behaviour and shows good agreement with the full-wave results. Similar responses under TE and TM polarizations demonstrate polarization-insensitive characteristics. The effects of stacking, linear displacement, air-gap separation, and rotation further show that interlayer coupling can be used to control the resonant response. Overall, the proposed structure provides a compact and flexible platform for wideband multi-notch microwave applications.

REFERENCES

[1] Holloway, C. L., Kuester, E. F., Gordon, J. A., O'Hara, J., Booth, J., & Smith, D. R. (2012). An overview of the theory and applications of metasurfaces: The two-dimensional equivalents of metamaterials. *IEEE antennas and propagation magazine*, *54*(2), 10-35.

[2] Smith, D. R., Padilla, W. J., Vier, D. C., Nemat-Nasser, S. C., & Schultz, S. (2000). Composite medium with simultaneously negative permeability and permittivity. *Physical review letters*, *84*(18), 4184.

[3] Baena, J. D., Bonache, J., Martín, F., Sillero, R. M., Falcone, F., Lopetegi, T., ... & Sorolla, M. (2005). Equivalent-circuit models for split-ring resonators and complementary split-ring resonators coupled to planar transmission lines. *IEEE transactions on microwave theory and techniques*, *53*(4), 1451-1461.

[4] Durán-Sindreu, M., Naqui, J., Bonache, J., & Martin, F. (2012). Split rings for metamaterial and microwave circuit design: A review of recent developments. *International Journal of RF and Microwave Computer-Aided Engineering*, *22*(4), 439-458.

[5] Bilotti, F., Toscano, A., Vegni, L., Aydin, K., Alici, K. B., & Ozbay, E. (2007). Equivalent-circuit models for the design of metamaterials based on artificial magnetic inclusions. *IEEE transactions on microwave theory and techniques*, *55*(12), 2865-2873.

[6] Marcelli, R. (2024). Equivalent circuits for microwave metamaterial planar components. *Sensors*, *24*(7), 2212.

[7] Almuhlafi, A. M., Alshaykh, M. S., Alajmi, M., Alshammari, B., & Ramahi, O. M. (2024). A microwave differential dielectric sensor based on mode splitting of coupled resonators. *Sensors*, *24*(3), 1020.

[8] Katoch, K., Jaglan, N., Kanaujia, B. K., Chen, P. Y., & Kishk, A. A. (2024). Triple bandstop 2.5 D frequency selective surface for sub-6 GHz 5G communication. *IEEE Transactions on Electromagnetic Compatibility*, *66*(5), 1420-1429.

[9] Yan, M., Xiu, X., Liu, J., Chen, H., Feng, S., Xue, Q., & Che, W. (2024). Polarization-insensitive high-angular stable frequency selective surfaces based on anisotropic artificial electromagnetic medium. *IEEE Transactions on Microwave Theory and Techniques*, *73*(2), 1094-1104.

[10] Ye, H., Wei, J., Lin, L., Liu, F., Miao, L., Bie, S., & Jiang, J. (2020). A frequency-selective surface rasorber based on four functional layers. *IEEE Transactions on Antennas and Propagation*, *69*(5), 2768-2778.

[11] Grover, F. W. (2004). *Inductance calculations: working formulas and tables*. Courier Corporation.

[12] Garg, R., & Bahl, I. J. (2024). *Microstrip lines and slotlines*. Artech house.

[13] Sydoruk, O., Tatartschuk, E., Shamonina, E., & Solymar, L. (2009). Analytical formulation for the resonant frequency of split rings. *Journal of applied physics*, *105*(1).

[14] García-García, J., Martin, F., Falcone, F., Bonache, J., Gil, I., Lopetegi, T., ... & Marqués, R. (2004). Spurious passband suppression in microstrip coupled line band pass filters by means of split ring resonators. *IEEE Microwave and Wireless Components Letters*, *14*(9), 416-418.

[15] Naji, A., & Soliman, M. H. (2017). Center frequency stabilization in planar dual-mode resonators during mode-splitting control. *Scientific Reports*, *7*(1), 43855.

[16] Hong, J. S., & Lancaster, M. J. (2011). *Microstrip filters for RF/microwave applications* (Vol. 656). New York: wiley.

[17] Penciu, R. S., Aydin, K., Kafesaki, M., Koschny, T., Ozbay, E., Economou, E. N., & Soukoulis, C. M. (2008). Multi-gap individual and coupled split-ring resonator structures. *Optics express*, *16*(22), 18131-18144.

[18] Ermiş, S. (2026). Tunable multiband metamaterial absorber with polarization sensitivity via multi-tier strip modifications for millimeter-Wave applications. *Applied Physics A*, *132*(4), 297.

[19] Faruque, M. R. I., Idrus, I. N., Abdullah, S., Ramachandran, T., Siddiky, A. M., Al-mugren, K. S., & Hossain, M. J. (2025). Crossed metal SRR metamaterial with high impact factor for satellite frequency applications. *Applied Physics A*, *131*(7), 544.

[20] Cheng, Y., Nie, Y., Wang, X., & Gong, R. (2013). An ultrathin transparent metamaterial polarization transformer based on a twist-split-ring resonator. *Applied Physics A*, *111*(1), 209-215.

[21] Carver, J., Reignault, V., & Gadot, F. (2014). Engineering of the metamaterial-based cut-band filter. *Applied Physics A*, *117*(2), 513-516.

[22] Hong, J. S. (2000). Couplings of asynchronously tuned coupled microwave resonators. *IEE Proceedings-Microwaves, Antennas and Propagation*, *147*(5), 354-358.

[23] Su, L., Naqui, J., Mata-Contreras, J., & Martín, F. (2014). Modeling metamaterial transmission lines loaded with pairs of coupled split-ring resonators. *IEEE Antennas and Wireless Propagation Letters*, *14*, 68-71.

[24] Siddiky, A. M., Faruque, M. R. I., Islam, M. T., & Abdullah, S. (2021). A multi-split based square split ring resonator for multiband satellite applications with high effective medium ratio. *Results in Physics*, *22*, 103865.

[25] Assimonis, S. D., & Fusco, V. (2019). Polarization insensitive, wide-angle, ultra-wideband, flexible, resistively loaded, electromagnetic metamaterial absorber using conventional inkjet-printing technology. *Scientific reports*, *9*(1), 12334.

[26] Rahman, A. A. M., Islam, M. T., Moniruzzaman, M., Misran, N., Alorifi, F., Shamsan, Z. A., ... & Soliman, M. S. (2023). Triple band frequency tunable polarization insensitive metamaterial absorber for WLAN and 5G applications. *Optical Materials*, *145*, 114368.

[27] Hakim, M. L., Alam, T., Islam, M. T., Alsaif, H., & Soliman, M. S. (2023). Polarization-independent fractal square splits ring resonator (FSSRR) multiband metamaterial absorber/artificial magnetic conductor/sensor for Ku/K/Ka/5G (mm-Wave) band applications. *Measurement*, *210*, 112545.

[28] Hakim, M. L., Alam, T., Soliman, M. S., Sahar, N. M., Baharuddin, M. H., Almalki, S. H., & Islam, M. T. (2022). Polarization insensitive symmetrical structured double negative (DNG) metamaterial absorber for Ku-band sensing applications. *Scientific reports*, *12*(1), 479.

[29] Islam, M. R., Islam, M. T., Moniruzzaman, M., Samsuzzaman, M., & Arshad, H. *Penta band single negative meta-atom absorber designed on square enclosed star-shaped modified split ring resonator for S-, C-, X-and Ku-bands microwave applications. Sci. Rep. 11, 8784 (2021)*.

[30] Baqir, M. A., Latif, H., Altintas, O., Akhtar, M. N., Karaaslan, M., Server, H., ... & Idrees, N. M. (2022). Fractal metamaterial based multiband absorber operating in 5G regime. *Optik*, *266*, 169626.